Radial Velocity Estimation of Ships on Open Sea in the Azimuth Multichannel SAR System

Junying Yang, Xiaolan Qiu, *Member, IEEE*, Mingyang Shang, Shouye Lv, Lihua Zhong, and Chibiao Ding

***Abstract*—The azimuth multichannel synthetic aperture radar (SAR) system can meet the requirements of high resolution and wide swath (HRWS) simultaneously, which overcomes the constraint of the traditional single-channel SAR. However, for a moving target illuminated by the azimuth multichannel SAR system, its radial velocity will lead to ambiguous components and mislocation in the image. Therefore, the radial velocity estimation plays an important role in improving the image quality and moving target relocation, especially for large ships on the open sea. However, as the pulse repetition frequency of a single channel is less than the Doppler spectrum, the traditional velocity estimation methods working in the image domain are out of action. This article suggests an idea that the issue of velocity estimation is converted into that of the linear phase errors estimation combining the linear fitting method, and it is assumed that the target has been already detected before applying the velocity estimation algorithms. To estimate the linear phase errors, two algorithms operating in the Doppler domain are introduced and compared, namely the subspace-based method and the modified frequency correlation method. The advantages of the proposed approaches are free from iteration operation and high accuracy. Besides, the effectiveness of the methods is demonstrated via simulation data and GaoFen-3 real data from ultra-fine stripmap mode. Finally, this article analyzes the velocity estimation accuracy of the two methods and the influence of channel imbalance through substantial experiments.**

***Index Terms*—Azimuth multichannel, high resolution and wide swath (HRWS), radial velocity estimation, synthetic aperture radar (SAR).**

Manuscript received October 13, 2020; revised November 19, 2020, January 11, 2021, and February 14, 2021; accepted March 22, 2021. Date of publication March 24, 2021; date of current version April 14, 2021. This work was supported in part by the National Science Foundation of China under Grant 61991421 and Grant 61725105. *(Corresponding author: Junying Yang.)*

Junying Yang, Xiaolan Qiu, and Mingyang Shang are with the Key Laboratory of Technology in Geo-Spatial Information Processing and Application Systems, Chinese Academy of Sciences, Beijing 100190, China, with the Aerospace Information Research Institute, Chinese Academy of Sciences, Beijing 100094, China, and also with the School of Electronic, Electrical and Communication Engineering, University of Chinese Academy of Sciences, Beijing 100049, China (e-mail: yangjunying17@mails.ucas.edu.cn; xlqiu@mail.ie.ac.cn; shangmingyang16@mails.ucas.edu.cn).

Shouye Lv is with the Institute of Remote Sensing Information, Beijing 100192, China (e-mail: lvshouye@126.com).

Lihua Zhong is with the Key Laboratory of Technology in Geo-Spatial Information Processing and Application Systems, Chinese Academy of Sciences, Beijing 100190, China, and also with the Aerospace Information Research Institute, Chinese Academy of Sciences, Beijing 100094, China (e-mail: lhzhong@mail.ie.ac.cn).

Chibiao Ding is with the Key Laboratory of Technology in Geo-Spatial Information Processing and Application Systems, Chinese Academy of Sciences, Beijing 100190, China, with the Aerospace Information Research Institute, Chinese Academy of Sciences, Beijing 100094, China, with the National Key Laboratory of Microwave Imaging Technology, Beijing 100190, China, and also with the School of Electronic, Electrical and Communication Engineering, University of Chinese Academy of Sciences, Beijing 100049, China (e-mail: cbding@mail.ie.ac.cn).

Digital Object Identifier 10.1109/JSTARS.2021.3068573

I. Introduction

FOR traditional single-channel synthetic aperture radar (SAR), there is inevitably a tradeoff between high resolution and wide swath (HRWS). Because they have completely different requirements for the system pulse repetition frequency (PRF). One of the technologies that can achieve HRWS imaging is to employ multiple channels to receive signals along the azimuth direction simultaneously [1]–[3]. At present, there have been several in-orbit multichannel SAR sensors in the world, for example, TerraSAR-X launched in June 2007 by Germany [4], RadarSat-2 launched in December 2007 by Canada [5], and ALOS-2 launched in May 2014 by Japan [6]. Besides, GaoFen-3 (GF-3), launched in August 2016, is the first Chinese multichannel SAR sensor working in the ultra-fine stripmap (UFS) mode (or named dual receiving channel mode) [7]. It allows for a reduced PRF on transmitting to guarantee a wide swath. However, high azimuth resolution usually corresponds to a large Doppler bandwidth [8]. In order to satisfy Nyquist Theorem, the echoes from multiple channels are equivalent to a single-channel echo of an increased effective sampling rate with additional digital processing on receiving. Moreover, the multiple of the PRF increase is equal to the number of channels. Typically, the preprocessing techniques before imaging include channel imbalance calibration [9]–[11] and unambiguous spectrum reconstruction [12], [13]. For a scene containing no moving targets, an HRWS product is obtained after the imaging algorithm.

Whereas the moving target imaging has been a subject of longstanding concern, whose key is to compensate for the relative movement of the moving target and radar platform. Unfortunately, we know nothing about the movement of noncooperative targets. It is exactly what causes the moving target smeared and mislocated on the image [14]–[16]. Besides, for the azimuth multichannel SAR system, the motion of targets will also cause particular azimuth ambiguity, which is reflected in the image as several pairs of false targets [17], [18]. Especially for large ships on the open sea, false targets will increase the false alarm rate of target detection. Therefore, velocity estimation plays a crucial role in improving the image quality and moving target relocation. The velocity of the target can be decomposed into radial velocity and along-track velocity generally. The radial velocity leads to the dislocation as well as azimuth ambiguity in the image, while the along-track velocity mainly causes the unfocused moving target image. There have been many well-established methods to refocus the target operating in the image domain conveniently [19], [20]. Therefore, estimating the radial velocity in the echo

domain has always been the focus of researchers. The roles of the radial velocity estimation are summarized as follows.

1) The offset of the target along the azimuth direction in the image is proportional to its radial velocity, and the correct estimation results can be used to relocate the target.
2) The design of the moving target reconstruction filter depends on the radial velocity. The estimation results are conducive to reconstruct the unambiguous Doppler spectrum [21].
3) The radial velocity will introduce some undesired phase terms, and compensation for these phase terms helps realize the integrated imaging processing of moving targets and static scenes simultaneously [17].

For the azimuth multichannel SAR system, since the PRF of a single channel is less than the Doppler bandwidth of the signal, it is impossible to image the echoes of multiple channels separately. Therefore, the traditional velocity estimation methods working in the image domain are out of action. Many researchers have worked on estimating the radial velocity of the target illuminated by the azimuth multichannel SAR system. Some of the available methods have a great computational burden due to the inevitable iterative operation. An algorithm in [22] based on the phase mismatch on the range frequency was suggested to estimate the radial velocity. However, the phase mismatch value is obtained by multiple iterations based on minimum entropy. In [23], the authors estimated the radial velocity by a group of matched reconstruction filter banks, which is also a searching and iteration operation. Besides, in [24], the authors applied the maximum likelihood method to estimate the cone angle as well as the radial velocity. In essence, it is also an iterative process. Also, there are some more efficient algorithms to avoid iteration. In [25], the radial velocity of the moving target is obtained by estimating the direction-of-arrival (DOA) of the signal. Due to the Doppler spectrum ambiguity, the number of the estimated DOAs is M. M is the number of the main Doppler spectrum ambiguity. The results of radial velocity estimation need to be calculated from the estimated M DOAs. And the number of the estimated DOAs will be $2M$ if the effect of the clutter is not ignorable. In addition, there is a velocity estimation method with the help of the amplitude information of the range cell migration (RCM) curve of the moving target [26]. It is based on the fact that the RCM curve is not subject to PRF limitations. The unambiguous radial velocity is estimated by Radon transform in the compressed range domain. However, this method is not suitable for the spaceborne SAR sensor and does not make full use of multichannel information. Furthermore, for multichannel systems, an inevitable thing is the existence of channel errors. As far as the author knows, there are few published pieces of literature to analyze the influence of such channel imbalance on velocity estimation quantitatively.

This article suggests an idea that the issue of velocity estimation is converted into that of the linear phase errors estimation combining the linear fitting method. To estimate the linear phase errors, this article employs two algorithms, i.e., the subspace-based method (SBM) and the modified frequency correlation method (MFCM). For the SBM, Li and Yang proposed the orthogonal subspace method (OSM) and the signal subspace comparison method (SSCM) for the first time to estimate the phase imbalance between channels, but they did not discuss the issue of moving targets [9], [10]. Inspired by them, we employ the SBM combined with the linear fitting technique to estimate the radial velocity of moving targets. In order to adapt to different needs in engineering implementation, we propose a thought of intercepting the signal near the azimuth zero frequency and obtain a robust estimation through the correlation method, i.e., MFCM. The advantages of the two algorithms are free from the iterative process, making full use of multichannel information, and having a strong anti-interference ability. Besides, another contribution of this article is that we analyzed the velocity estimation accuracy of the two methods and pointed out which method has better performance in different application scenarios. And in this article, the influence of channel imbalance on velocity estimation and both them on image quality are analyzed for the first time.

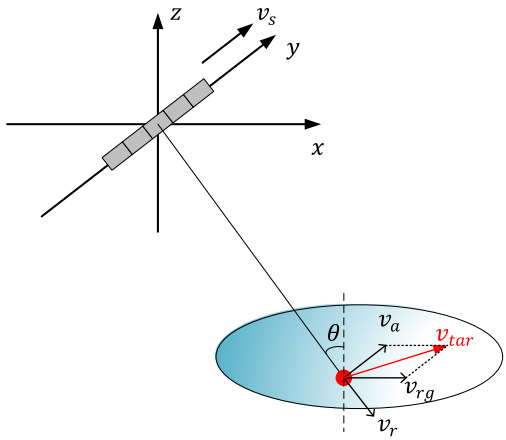

Fig. 1. Geometry of an azimuth multichannel SAR imaging system.

It is worth mentioning that velocity estimation methods will apply to the speed measurement of ships with a high signal-to-clutter ratio (SCR) on the open sea. And it is assumed that the target has been already detected before applying the velocity estimation algorithms. But the moving target detection, which is a tough problem in general, is not involved in this article.

The rest of this article is organized as follows. In Section II, we first formulate the problem. The proposed two algorithms are described in detail in Section III. Some simulation and real-data experiments are designed in Section IV to verify the effectiveness of the proposed methods. Then, the performance analysis of the proposed method is shown in Section V. Finally, some conclusions and the outlook are given in Section VI.

II. Mathematical Relationship Model

The geometry of the azimuth multichannel SAR system is shown in Fig. 1. The y-axis is in the direction of the platform velocity v_s, and the z-axis is away from the Earth's center. The x-axis completes the orthogonal right-handed frame. The altitude of the platform flight is H. We consider a moving target with velocity v_{tar} whose incidence angle is θ. In general, the velocity v_{tar} is decomposed into the along-track velocity v_a

and the cross-track velocity v_{rg}. The radial velocity v_r we are concerned about is the projection of the cross-track velocity v_{rg} on the slant range direction. As far as the spaceborne SAR system is concerned, the synthetic aperture time is short. Thus, we assume that the radial velocity is a constant value during continuous illumination. Take the GF-3 SAR sensor operating in the C-band as an example. If the reference slant range is 800 km, the synthetic aperture time is 1.58 s. In such a short time interval, it is reasonable to ignore the acceleration of the target.

During the system operation, the reference phase center transmits the signal (the first channel is usually regarded as a reference channel). All the subapertures receive the echoes simultaneously and separately. For the convenience of description, researchers often convert the model of one transmitter and multiple receivers into the model of multiple self-transmitting and self-receiving phase centers by compensating for a constant phase term [18]–[27]. And the distance between two adjacent effective phase centers (EPC) reduces to half of that between two actual phase centers (APC). It is assumed that the coordinates of the reference channel and the target are $(0, 0, H)$ and $(x_0, y_0, 0)$ respectively at the initial time. Therefore, at a certain azimuth time η, the instantaneous slant range between the nth EPC and the moving target can be expressed as (1)–(5) shown at the bottom of this page, where η_c is the value related to the initial coordinates of the target, and $T_d = d/2v_s$ is the time delay between adjacent EPCs. Let $R_0 = \sqrt{H^2 + x_0^2}$ as the shortest slant range of the target. And $x_0/\sqrt{H^2 + x_0^2}$ represents the sine of the incident angle θ. However, $v_{rg}\sin\theta$ is exactly the radial velocity of the target. Then, the simplified form of (1) is written as (2)

It is assumed that the operating frequency of the radar is f_0, and the chirp rate of its transmission signal is K_r. The speed of light is represented by c. The echo received by the nth channel is expressed as (3), where $\sigma(x_0, y_0)$ is the complex constant related to the reflection coefficient of the moving target. $\omega_r(\cdot)$ and $\omega_a(\cdot)$ are the antenna patterns in the range and azimuth directions, respectively. And τ is the time in range direction. After down-conversion and range compression (RC), the received echo becomes (4). T_p and B_r represent the pulsewidth and bandwidth of the transmitted signal, respectively. And the wavelength of the carrier is λ. Substitute (2) into (4), the echo of the nth channel in the range-Doppler domain is expressed as (5), where $W_{fa}(\cdot)$ represents the envelope of the azimuth antenna pattern in the frequency domain. f_t and K_a are Doppler parameters closely related to the target motion shown in (6) and (7)

$$f_t = \frac{2v_r}{\lambda} \tag{6}$$

$$K_a = -\frac{2(v_s - v_a)^2}{\lambda R_0}. \tag{7}$$

Since the PRF of a single channel is much less than the Doppler bandwidth of the signal, Doppler ambiguity occurs in each channel. The number of the main doppler spectrum ambiguity is calculated by

$$N_{ambi} = \text{floor}\left(\frac{B_a}{f_p}\right) = 2L + 1. \tag{8}$$

For simplicity in expression, we define it as an odd number. But there is no restriction that it must be an odd number.

Therefore, for a stationary target ($v_r = 0,\ v_a = 0$), the relationship between nth channel and the first channel (reference channel) can be expressed in the Doppler domain as

$$S_n(\tau, f_a) = \sum_{l=-L}^{l=L} S_1(\tau, f_a + l \cdot f_p) \exp(j\phi_{l,n}), \quad -f_p/2 \le f_a \le f_p/2. \tag{9}$$

$$R_n(\eta) = \sqrt{H^2 + (x_0 + v_{rg}\eta)^2} + \left((v_s - v_a)\eta + \frac{(n-1)d}{2} - y_0\right)^2 \tag{1}$$

$$\approx \sqrt{H^2 + x_0^2} + \frac{x_0}{\sqrt{H^2 + x_0^2}} v_{rg}(\eta - \eta_c) + \frac{(v_s - v_a)^2}{2\sqrt{H^2 + x_0^2}} (\eta - \eta_c + (n-1)T_d)^2$$

$$R_n(\eta) = R_0 + v_r(\eta - \eta_c) + \frac{(v_s - v_a)^2}{2R_0}(\eta - \eta_c + (n-1)T_d)^2 \tag{2}$$

$$s_n(\tau, \eta) = \sigma(x_0, y_0)\,\omega_r\left(\tau - \frac{2R_n(\eta)}{c}\right)\omega_a(\eta - \eta_c + (n-1)T_d)\exp\left(j2\pi f_0\tau - \frac{2R_n(\eta)}{c} + j\pi K_r\left(\tau - \frac{2R_n(\eta)}{c}\right)^2\right) \tag{3}$$

$$s_n(\tau, \eta) = \sigma(x_0, y_0)\,T_p \text{sinc}\left\{B_r\left(\tau - \frac{2R_n(\eta)}{c}\right)\right\}\omega_a(\eta - \eta_c + (n-1)T_d)\exp\left(-j \cdot \frac{4\pi}{\lambda} R_n(\eta)\right) \tag{4}$$

$$S_n(\tau, f_a) = \tilde{\sigma}\,\text{sinc}\left\{B_r\left(\tau - \frac{2R_n(f_a)}{c}\right)\right\} W_{f_a}(f_a - f_t) \cdot \exp\left(-j\frac{4\pi}{\lambda}R_0\right)\exp(-j2\pi f_a\eta_c)\exp\left(-j\pi\frac{(f_a - f_t)^2}{K_a}\right)\exp(j2\pi f_t(n-1)T_d)\exp(j2\pi f_a(n-1)T_d). \tag{5}$$

TABLE I
MEANING OF THE NOTATIONS IN THIS ARTICLE

Symbol	Quantity
N	The number of channels;
n	Index of the receive channels, $n = 1,2\cdots\cdots,N$;
τ	Range time;
η	Azimuth time;
f_a	Azimuth Doppler frequency;
f_p	Pulse repetition frequency of a single channel;
d	Distance between adjacent APCs;
v_s	Platform velocity;
T_d	Time delay between adjacent EPCs, $T_d = d/2v_s$;
l	Index of Doppler ambiguity component;
B_a	Doppler spectrum bandwidth of the target;
θ	The incidence angle of the target;
H	The altitude of the platform;
N_{ambi}	The number of the main doppler spectrum ambiguity, $N_{ambi} = 2L + 1 = floor(B_a/f_p)$;
λ	Wavelength of the radar signal;
f_t	Doppler shift caused by radial velocity;
v_r	Radial velocity of the moving target;
$(\cdot)^T$	The vector transpose operation;
$(\cdot)^H$	The vector conjugate-transpose operation;
$diag\{\boldsymbol{a}\}$	Diagonal matrix with the elements of vector $\boldsymbol{a}$ on its diagonal;
$vec\{\boldsymbol{A}\}$	Vector formed from the diagonal elements of square matrix $\boldsymbol{A}$;
$ang\{\cdot\}$	The phase of complex value;
$\frac{\boldsymbol{a}}{\boldsymbol{b}}$	Vectors $\boldsymbol{a}$ and $\boldsymbol{b}$ are divided by the corresponding elements.

where

$$\phi_{l,n} = 2\pi\left(f_a + l \cdot f_p\right)(n-1)\,T_d. \tag{10}$$

For the sake of convenience, $S_{1,l}(f_a)$ is used to stand for $S_1(\tau, f_a + l \cdot f_p)$, and the notations of the parameters used in this article are summarized in Table I. The signal of a stationary target with the additive complex white noise using vector notation can be written as

$$\boldsymbol{S}_{static} = \boldsymbol{A}\boldsymbol{S}_1 + \boldsymbol{N}. \tag{11}$$

where

$$\boldsymbol{S}_{static} = \left[S_1(\tau, f_a),\ S_2(\tau, f_a), \ldots, S_N(\tau, f_a)\right]^T \tag{12}$$

$$\boldsymbol{S}_1 = \left[S_{1,-L}(f_a), S_{1,-L+1}(f_a), \ldots,\ S_{1,L}(f_a)\right]^T \tag{13}$$

$$\boldsymbol{A} = \left[\boldsymbol{\Phi}_{-L}(f_a),\ \boldsymbol{\Phi}_{-L+1}(f_a), \ldots,\ \boldsymbol{\Phi}_{L}(f_a)\right] \tag{14}$$

$$\boldsymbol{\Phi}_l\ (f_a) = \left[\phi_{l,1}, \phi_{l,2}, \ldots, \phi_{l,N}\right]^{\boldsymbol{T}} \tag{15}$$

$$\boldsymbol{N} = \left[N_1(\tau, f_a),\ N_2(\tau, f_a), \ldots, N_N(\tau, f_a)\right]^T. \tag{16}$$

For a moving target, the influence of its radial velocity is reflected in two aspects. On the one hand, the RCM curve and Doppler shift f_t caused by the radial velocity are different from those of the stationary target, which is illustrated in Fig. 2. Fig. 2(a) and (c) shows the RCM curves of the stationary target and the moving target in the Doppler domain in the conventional single-channel SAR system respectively. We assume that the Doppler center frequency of the stationary target is zero. The difference between them is the Doppler shift caused by the radial velocity of the moving target, which makes its Doppler center frequency no longer consistent with that of the stationary target. For the azimuth multichannel SAR system, the part of the spectrum outside $[-f_p/2,\ f_p/2]$ will also be folded into the frequency range, which is shown in Fig. 2(b) and (d). However, the above-mentioned influence is consistent in each channel. On the other hand, the radial velocity also results in the channel imbalance according to the phase term marking in the red square in (5), which is the core concept of the article. Therefore, the signal of a moving target can be expressed as

$$\boldsymbol{S}_{moving} = \boldsymbol{\Gamma}(v_r)\,\boldsymbol{A}\boldsymbol{S}_1 + \boldsymbol{N} \tag{17}$$

where

$$\boldsymbol{\Gamma}\ (v_r) = diag\left\{1, \exp(j\Delta), \ldots, \exp\left(j(N-1)\Delta\right)\right\} \tag{18}$$

$\Delta = 2\pi T_d \frac{2v_r}{\lambda}$.

The RCM curve and Doppler shift caused by the radial velocity are included in $\boldsymbol{S}_1$, while $\boldsymbol{\Gamma}(v_r)$ represents the imbalance of the channels. Comparing (11) with (17), the phase terms caused by radial velocity are equivalent to particular linear phase errors. In this article, we estimate the linear phase errors as well as the radial velocity.

III. RADIAL VELOCITY ESTIMATION METHODS

In Section II, the phase terms caused by the radial velocity are modeled as linear phase errors. At present, the subspace methods, including the OSM and SSCM, are commonly used to estimate the phase imbalance between channels. The two algorithms are both based on the properties of subspace, so they are collectively referred to as the SBM in this article. Combining the linear fitting method, the radial velocity of the moving target is estimated. One of the characteristics of the SBM is that the number of the main doppler spectrum ambiguity needs to be known accurately, but in the engineering implementation, it can not be judged accurately when the signal to clutter ratio is low. Moreover, it also cannot be calculated by (8) because of the uncertainty of the signal bandwidth. Thus, we propose a second radial velocity method called the MFCM. This section will describe the SBM in Section III-A and B, and the MFCM will be introduced in Section III-C.

A. Signal Subspace Method

This section starts with a brief overview of the signal subspace method in [10]. Assuming that the additive noise at each channel is independent and identically distributed, the covariance matrix of (17) can be formulated as

$$\begin{aligned}\boldsymbol{R} &= E\left\{\boldsymbol{S}_{moving}\boldsymbol{S}_{moving}^H\right\} \\ &= E\left\{\left[\boldsymbol{\Gamma}(v_r)\,\boldsymbol{A}\boldsymbol{S}_1 + \boldsymbol{N}\right]\left[\boldsymbol{\Gamma}(v_r)\,\boldsymbol{A}\boldsymbol{S}_1 + \boldsymbol{N}\right]^H\right\} \\ &= \boldsymbol{\Gamma}(v_r)\,\boldsymbol{A}\cdot E\left\{\boldsymbol{S}_1\boldsymbol{S}_1^H\right\}\cdot\boldsymbol{A}^H\boldsymbol{\Gamma}^{\mathrm{H}}(v_r) + \sigma^2\boldsymbol{I}_N.\end{aligned} \tag{19}$$

where σ^2 is the noise power, and $\boldsymbol{I}_N$ is the N-dimensional identity matrix. In practical terms, the statistical covariance

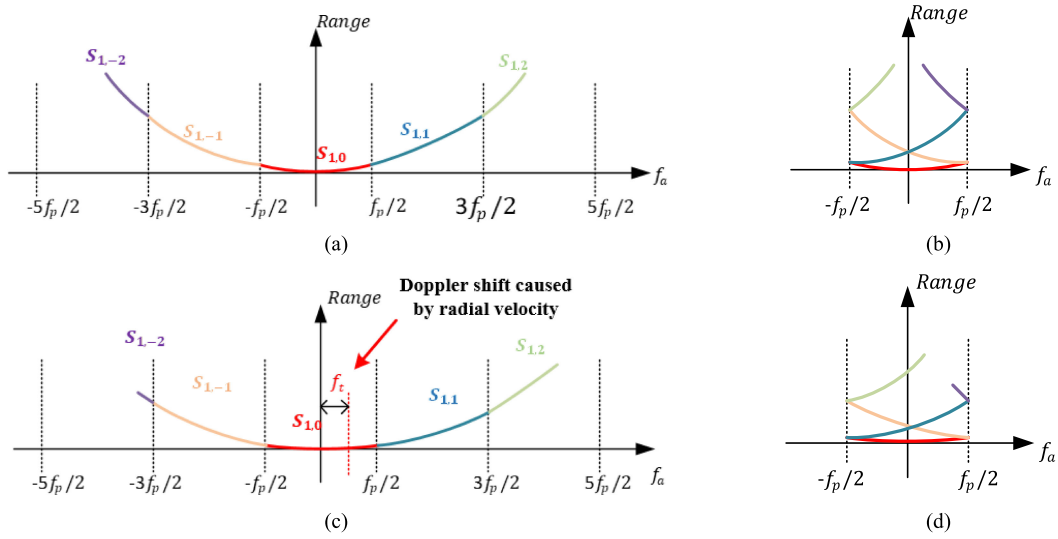

Fig. 2. RCM curve in range-Doppler domain. (a) RCM curve in the conventional single-channel SAR system. (b) RCM curve of stationary target in the azimuth multichannel SAR system. (c) RCM curve of moving target in the conventional single-channel SAR system. (d) RCM curve of moving target in the azimuth multichannel SAR system.

matrix $\boldsymbol{R}$ is estimated by the sample covariance matrix $\tilde{\boldsymbol{R}}$ with N_s range bins (read formula (44) in [9] and formula (33) in [10] for reference).

Decomposing $\boldsymbol{R}$ in (19), we get the results as

$$\boldsymbol{R} = \boldsymbol{U}\boldsymbol{\Lambda}\boldsymbol{U}^H = \boldsymbol{U_s}\,\boldsymbol{\Lambda_s}\boldsymbol{U_s^H} + \boldsymbol{U_n}\boldsymbol{\Lambda_n}\boldsymbol{U_n^H} \tag{20}$$

where $\boldsymbol{\Lambda}$ is the eigenvalue matrix given by $\boldsymbol{\Lambda} = \mathrm{diag}\{\lambda_1, \lambda_2, \ldots, \lambda_{2L+1}, \ldots, \lambda_N\}$. And the eigenvalues meet $\lambda_1 \geq \lambda_2 \geq \cdots \geq \lambda_{2L+1} \gg \lambda_{2L+2} = \cdots = \lambda_N$. In this way, $\boldsymbol{\Lambda_s}$ and $\boldsymbol{U_s}$ are the signal eigenvalue matrix and the corresponding eigenvector matrix, where $\boldsymbol{\Lambda_s} = \mathrm{diag}\{\lambda_1, \lambda_2, \ldots, \lambda_{2L+1}\}$. Similarly, $\boldsymbol{\Lambda_n}$ and $\boldsymbol{U_n}$ are the noise eigenvalue matrix and the corresponding eigenvector matrix, where $\boldsymbol{\Lambda_s} = \mathrm{diag}\{\lambda_{2L+2}, \lambda_{2L+3}, \ldots, \lambda_N\}$. Then, the subspace spanned by the steering vectors is the same as that by the signal eigenvectors [28], [29], i.e.,

$$\mathrm{span}\ \{\boldsymbol{\Gamma}(v_r)\,\boldsymbol{A}\} = \mathrm{span}\,\{\boldsymbol{U_s}\}. \tag{21}$$

As we all know, the same subspaces have the same projection matrix. Therefore,

$$\boldsymbol{U_s}\left(\boldsymbol{U_s^H}\boldsymbol{U_s}\right)^{-1}\boldsymbol{U_s^H} = \boldsymbol{\Gamma}(v_r)\,\boldsymbol{A}\left(\boldsymbol{A^H}\boldsymbol{\Gamma^H}(v_r)\,\boldsymbol{\Gamma}(v_r)\,\boldsymbol{A}\right)^{-1}\boldsymbol{A^H}\boldsymbol{\Gamma^H}(v_r). \tag{22}$$

What is more, $\boldsymbol{U_s^H}\,\boldsymbol{U_s} = \boldsymbol{I}_{2L+1}$ and $\boldsymbol{\Gamma^H}(v_r)\boldsymbol{\Gamma}(v_r) = \boldsymbol{I}_N$. Let us define two matrices:

$$\boldsymbol{V} = \boldsymbol{U_s}\,\boldsymbol{U_s^H}, \tag{23}$$

$$\boldsymbol{Q} = \boldsymbol{A}\left(\boldsymbol{A^H}\boldsymbol{A}\right)^{-1}\boldsymbol{A^H}. \tag{24}$$

Then, we rewrite the (22) as

$$\boldsymbol{V} = \boldsymbol{\Gamma}(v_r)\,\boldsymbol{Q}\boldsymbol{\Gamma^H}(v_r). \tag{25}$$

The linear phase errors are given by

$$\mathrm{vec}\ (\boldsymbol{\Gamma}(v_r)) = \frac{\boldsymbol{V}(:\ 1)}{\boldsymbol{Q}(:\ 1)}. \tag{26}$$

where $\boldsymbol{V}(:\ 1)$ and $\boldsymbol{Q}(:\ 1)$ represent the first column of the respective matrix. From (18)

$$\mathrm{ang}\ (\mathrm{vec}\,(\boldsymbol{\Gamma}(v_r))) = [1,\ \Delta, \ldots, (N-1)\,\Delta]\ . \tag{27}$$

Consequently, the estimated radial velocity is determined by the linear fitting method [30]. The most common method of linear fitting is the least-squares method. The purpose is to minimize the sum of squared of errors between the predicted data and the actual data. We define two vectors: $\boldsymbol{x} = [01, \ldots, N-1]^T$ and $\boldsymbol{y} = [1, \Delta, \ldots, (N-1)\Delta]^T$. We predict the linear relationship between them is $\boldsymbol{y} = \hat{\Delta}\,\boldsymbol{x} + \boldsymbol{\varepsilon}$. Where $\boldsymbol{\varepsilon}$ is the error between the predicted data and the actual data. Thus, The linear fitting of the slope is estimated by

$$\hat{\Delta} = \min \varepsilon^T \varepsilon\ . \tag{28}$$

Then, we obtain the velocity by

$$\widehat{v_r} = \frac{\hat{\Delta}}{2\pi T_d}\cdot\frac{\lambda}{2}. \tag{29}$$

B. Noise Subspace Method

For the ships on the open sea, the clutter energy can be ignored. Thus, the subspace spanned by the steering vector is orthogonal to the noise subspace from [9], i.e.,

$$\mathrm{span}\,\{\boldsymbol{\Gamma}(v_r)\,\boldsymbol{A}\} \perp \mathrm{span}\,\{\boldsymbol{U_n}\}. \tag{30}$$

Since each column of the steering vector is orthogonal to the noise subspace, we define a cost function

$$J\ (v_r) = \min \sum_{i=-L}^{L} \left(\boldsymbol{\Gamma}(v_r)\,\boldsymbol{\Phi}_i\right)^H \boldsymbol{U_n}\boldsymbol{U_n^H}\left(\boldsymbol{\Gamma}(v_r)\,\boldsymbol{\Phi}_i\right)\ . \tag{31}$$

Because of the equivalence of mathematical expression, (31) can be rewritten as

$$J\ (v_r) = \min \boldsymbol{\delta}^H \boldsymbol{\Omega} \boldsymbol{\delta} \tag{32}$$

where

$$\boldsymbol{\Omega} = \left\{ \sum_{i=-L}^{L} \left(\text{diag}\left(\boldsymbol{\Phi}_i\right)\right)^H \boldsymbol{U_n} \boldsymbol{U_n}^H \left(\text{diag}\left(\boldsymbol{\Phi}_i\right)\right) \right\} \tag{33}$$

$$\boldsymbol{\delta} = vec\left(\boldsymbol{\Gamma}\left(v_r\right)\right). \tag{34}$$

The linear phase errors $\boldsymbol{\delta}$ are obtained by solving the following problem:

$$\begin{cases} \min \boldsymbol{\delta}^H \boldsymbol{\Omega} \boldsymbol{\delta} \\ \text{s.t. } \boldsymbol{\delta}^H \boldsymbol{\omega} \ = \ 1 \end{cases}. \tag{35}$$

When the first channel is taken as the reference channel, the weight vector $\boldsymbol{\omega}$ is expressed as $\boldsymbol{\omega} \ = [1, 0 \ldots, 0]^T$. The optimal solution of the above minimization problem is similar to that in space-time adaptive processing [31] as

$$\hat{\boldsymbol{\delta}} = \frac{\boldsymbol{\Omega}^{-1} \boldsymbol{\omega}}{\boldsymbol{\omega}^H \boldsymbol{\Omega}^{-1} \boldsymbol{\omega}}. \tag{36}$$

Then, we can obtain the radial velocity by the linear fitting method.

Although the principles of the signal subspace method and noise subspace method are different, they are both based on the properties of subspace, so they are collectively referred to as the SBM in this article.

C. Modified Frequency Correlation Method

From Fig. 2(c), in the conventional single-channel SAR system, PRF usually more than the Doppler bandwidth, which leads to no ambiguity component. While in the azimuth multichannel system, the Doppler bandwidth of the target usually is divided into N_{ambi} ambiguity components under the condition of low PRF illustrated as Fig. 2(d). If the synthetic aperture time of the target is artificially shortened (a small part of the RCM curve of the target is extracted), only one ambiguity component can be retained, as shown in Fig. 3. Here is a method of extracting a required small part RCM curve. For each target, we know the number of azimuth units occupied by its RCM curve, denoted as N_{all}. When the number of the main Doppler spectrum ambiguity is N_{ambi}, the length of the RCM curve corresponding to each ambiguity component is N_{all}/N_{ambi} approximately. If we employ the echo data near frequency zero to estimate the velocity, we only need to intercept a small part in the middle of the RCM curve. Specifically, the number of azimuth units we truncated N_{sub} should be less than N_{all}/N_{ambi}, and the cutout position should be in the center of the RCM curve.

We define the truncated multichannel echo vector as

$$\begin{aligned} \boldsymbol{S}'_{moving}\ (f_a) &= \ \boldsymbol{\Gamma}\left(v_r\right) \cdot \boldsymbol{\Phi}_0\left(f_a\right)\ S_{10}\left(f_a\right) \\ &= \boldsymbol{\Gamma}\left(v_r\right) \begin{bmatrix} S_1\left(\tau, f_a\right) \\ \exp\left(j2\pi f_a T_d\right) S_1\left(\tau, f_a\right) \\ \vdots \\ \exp\left(j2\pi f_a\left(N-1\right)\ T\_d\right) S_1\left(\tau, f_a\right) \end{bmatrix} \end{aligned} \tag{37}$$

where $\boldsymbol{S}'_{moving} = [S_1(\tau, f_a), S_2(\tau, f_a), \ldots, S_N(\tau, f_a)]^T$.

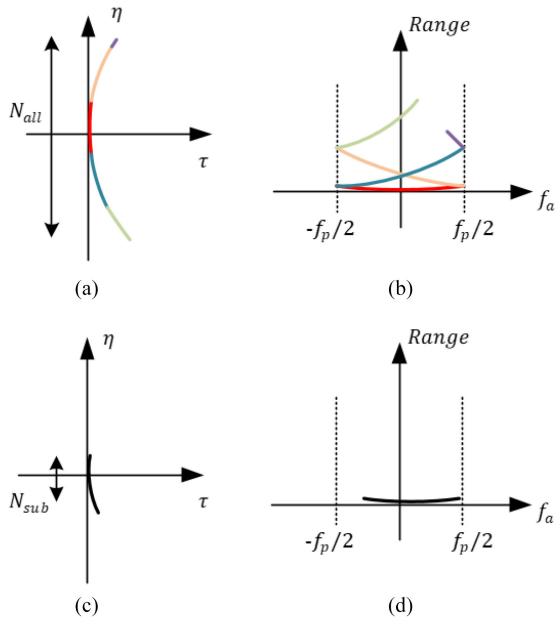

Fig. 3. Shortening the RCM curve in time domain is equivalent to shortening the Doppler bandwidth. (a) RCM curve of the moving target in time domain. (b) RCM curve in Doppler domain. (c) Partial RCM curve in time domain. (d) Partial RCM curve in Doppler domain.

From (37), the linear phase errors are calculated by

$$\begin{aligned} &vec\ \left(\boldsymbol{\Gamma}\left(v_r\right)\right) \\ &= \begin{bmatrix} S_1\left(\tau, f_a\right)/S_1\left(\tau, f_a\right) \\ S_2\left(\tau, f_a\right) \exp\left(-j2\pi f_a T_d\right)/S_1\left(\tau, f_a\right) \\ \vdots \\ S_N\left(\tau, f_a\right) \exp\left(-j2\pi f_a\left(N-1\right) T_d\right)/S_1\left(\tau, f_a\right) \end{bmatrix}. \end{aligned} \tag{38}$$

In the same way, the radial velocity can be obtained by the linear fitting method and (29). From (38), the same group of linear phase errors can be obtained by the signal of each azimuth frequency point, that is to say, the estimation result does not depend on the azimuth frequency point. Therefore, as long as a small part of the unambiguous azimuth spectrum is extracted, the estimation accuracy can be improved by averaging. For a spaceborne SAR system operating in the side-looking mode, there is little influence of Doppler center frequency. Even if the motion of the target will cause the cutout position at the center of the RCM curve not corresponding to the Doppler zero frequency, which is shown in Fig. 3(c), it does not affect us to extract the unambiguous azimuth spectrum of the moving targets except very fast ones.

IV. Experimental Results

A. Simulated HRWS SAR Data

To verify the effectiveness of the velocity estimation algorithms, the data of the experiment was obtained by a simulation four-channel spaceborne SAR sensor operating in C-band. The system works in the side-looking and strip-map mode. The baseline between two adjacent channels is 1.5 m. Besides, the first channel serves as the reference channel and transmits the

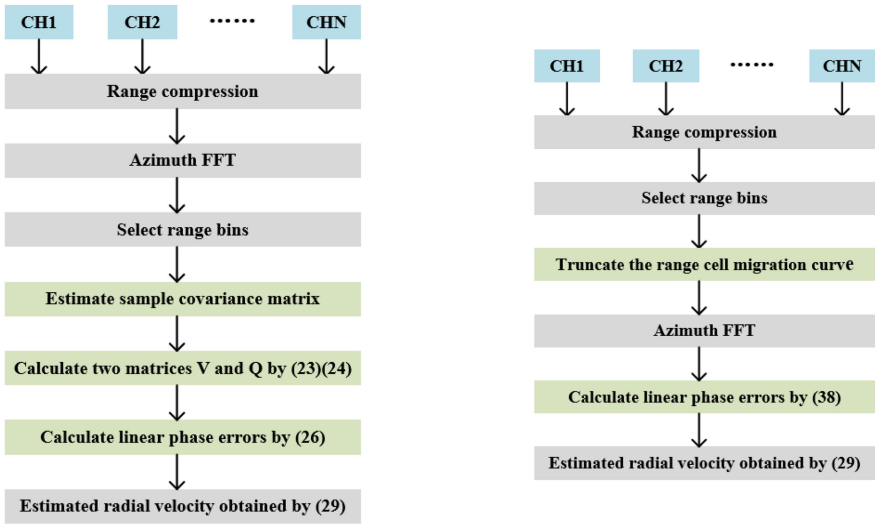

Fig. 4. (a) Simplified block diagram of the SBM. (b) Simplified block diagram of the MFCM.

signal, whose bandwidth, pulsewidth, and sampling rate are 120 MHz, 30 μs, and 150 MHz, respectively. The platform runs at a speed of 7500 m/s, and its reference slant range to the target is 700 km. Because the Doppler bandwidth of the moving target is 4000 Hz and the PRF of each channel is 1500 Hz, the Doppler ambiguity number is floor $(2.67) = 3$. Moreover, in the simulation scenario, we set a moving target with a radial velocity of 5 ms and its SCR is 30 dB.

The results from simulated data show that the signal subspace method and the noise subspace method get the same estimation results. Therefore, the SBM below refers to the signal subspace method. To describe the details, the block diagrams of the SBM and the MFCM are shown in Fig. 4. For sparsely distributed ships, it seems easy to "Select range bins." For the certain areas with relatively congested ships, we can extract the target energy in the coarse focus domain [17], so as to avoid many strong objects sharing the same part of range-Doppler data.

The estimation details of the two methods are displayed in Fig. 5. Fig. 5(a) shows the RCM curve of the simulated moving target, which can be obtained after moving target detection. And its azimuth spectrum is represented in Fig. 5(b). The phenomenon of azimuth ambiguity is apparent to the eye. For the SBM, we use 21 range bins to estimate the statistical covariance matrix and 1000 Doppler bins to improve the accuracy of estimation. The number of range bins used to estimate the statistical covariance matrix will affect the estimation result to a certain extent. But we concluded by an experiment: as long as the selected range bins contain 90% energy of the target, the estimation accuracy rate can reach 99.51%. That is why, we selected 21 range bins. Then, the linear phase errors calculated by (26) in each azimuth frequency are shown in Fig. 5(c). The linear fitting results of 1000 Doppler bins are recorded in Fig. 5(d). And the mean value is 4.986 m/s, which has an error of 0.014 m/s from the theoretical value of 5 m/s. For the MFCM, the truncated RCM curve and its unambiguous azimuth spectrum are shown in Fig. 5(e) and (f). In the main lobe, the number of azimuth units occupied by the RCM curve N_{all} is about 2100. The Doppler ambiguity number of this simulation experiment is 3, so the number of truncated azimuth units is no more than 700. In Fig. 5(e), $N_{sub} = 500$. The linear phase errors calculated by (38) in each azimuth frequency are shown in Fig. 5(g). The linear fitting results of 1000 Doppler bins are recorded in Fig. 5(h). Although the cutout position at the center of the RCM curve maybe not the beam center, it will not affect the estimation results just as Fig. 5(h). Similarly, the average of the estimation results of 1000 Doppler bins is taken as the final result, i.e., 4.9713 m/s. The difference between the estimated value and the ideal one is 0.0287 m/s. When SCR $= 30$ dB, the estimation error of SBM is slightly less than that of MFCM.

In addition, we recorded the running time of the two methods (on the following hardware: Intel i7 6700 CPU). Without parallel operations, the running time of estimating 100 targets' radial velocities with SBM is 73.27 s, and that of MFCM is 72.65 s. Therefore, the time for SBM and MFCM to estimate the radial velocity of a target is 0.733 s and 0.727 s, respectively. Since the two methods are free from iterative operations, the high execution efficiency is a significant advantage.

B. Real Data of GF-3 UFS Mode

GF-3 is the first Chinese multichannel SAR sensor working in the UFS mode. To verify the effectiveness of the proposed algorithms, we choose an ocean scene with seven moving vessels, shown in Fig. 6(a). Label the ships from left to right.

Without losing generality, we take the fifth moving target as an example to elaborate on the radial velocity estimation methods (Identify the 5th target according to the order of the targets' range bins). Since the energy of sea clutter is relatively weak, we can choose the range bins of the target directly, which is shown in Fig. 7(a). And Fig. 7(b) is the ambiguous Doppler spectrum of the fifth moving target. The number of samples to estimate the statistical covariance matrix is 31. In addition, we

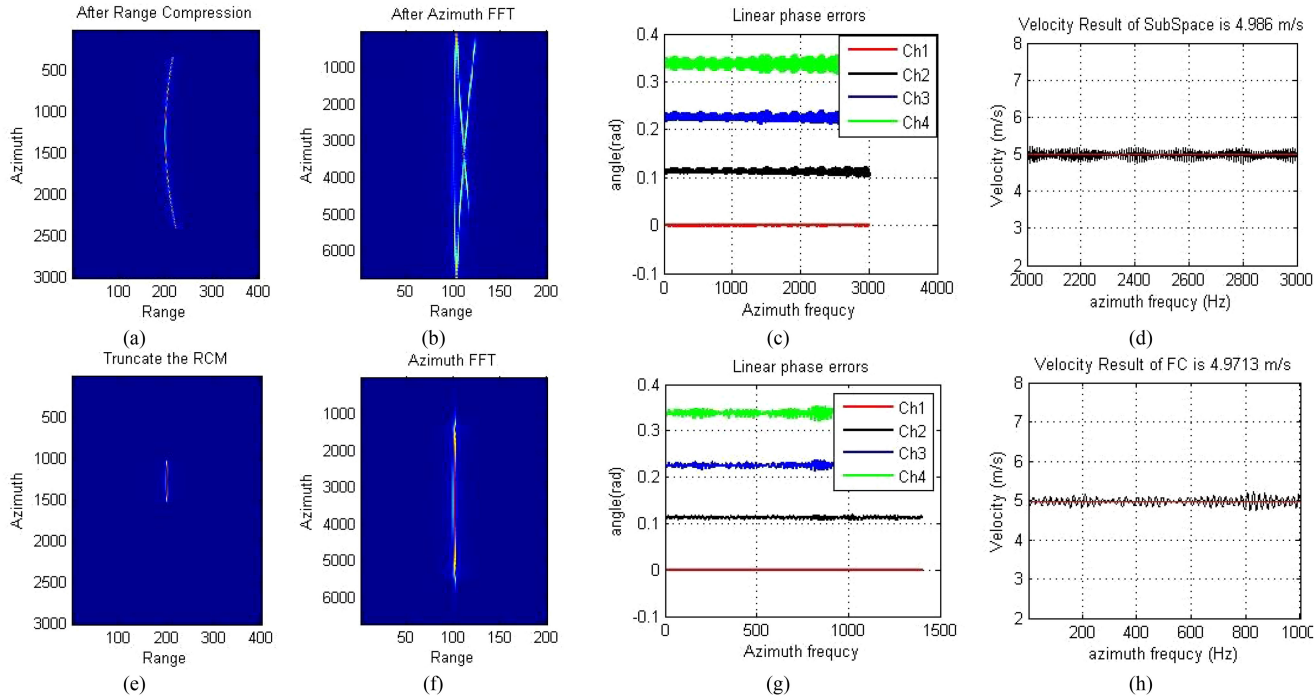

Fig. 5. SBM. (a) Truncation of the moving target after RC. (b) Azimuth spectrum of the moving target. (c) Linear phase errors estimated by SBM. (d) Mean radial velocity of 1000 Doppler bins, $v_r = 4.986$ m/s. MFCM. (e) Truncation of the RCM curve. (f) Azimuth spectrum of truncated moving target. (g) Linear phase errors estimated by MFCM method. (h) Mean radial velocity of 1000 Doppler bins, $v_r = 4.9713$ m/s.

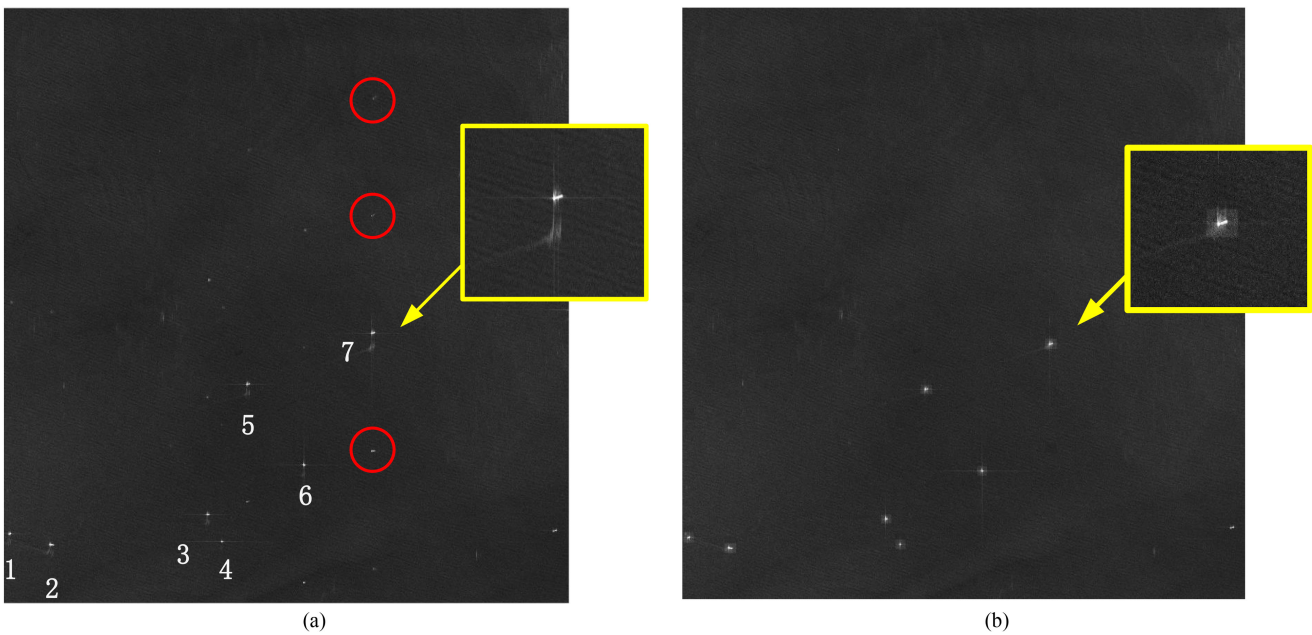

Fig. 6. (a) Original Imaging result of the ocean scene. (b) Imaging result after azimuth ambiguity suppression based on radial velocity estimation.

select 1000 Doppler bins to improve the accuracy of estimation by averaging. The linear phase errors and velocity estimations of each frequency point are shown in Fig. 7(c) and (d). The result tells that the radial velocity of the fifth moving targets is 3.43 m/s. For the MFCM, we first truncate the RCM curve of the target to obtain the unambiguous azimuth spectrum, as Fig. 7(e). In the main lobe, the number of azimuth units occupied by the RCM curve N_{all} is about 3500. In Fig. 7(e), $N_{sub} = 1200$. Likewise, we also select 31 rang bins and 1000 Doppler bins to improve the estimation accuracy. And its radial velocity is 3.38 m/s , which is very close to the result of SBM. Using the same process, we get the velocities of the other six moving targets and record them in Table II. At the same time, the SCRs of each ship in the RC domain are measured.

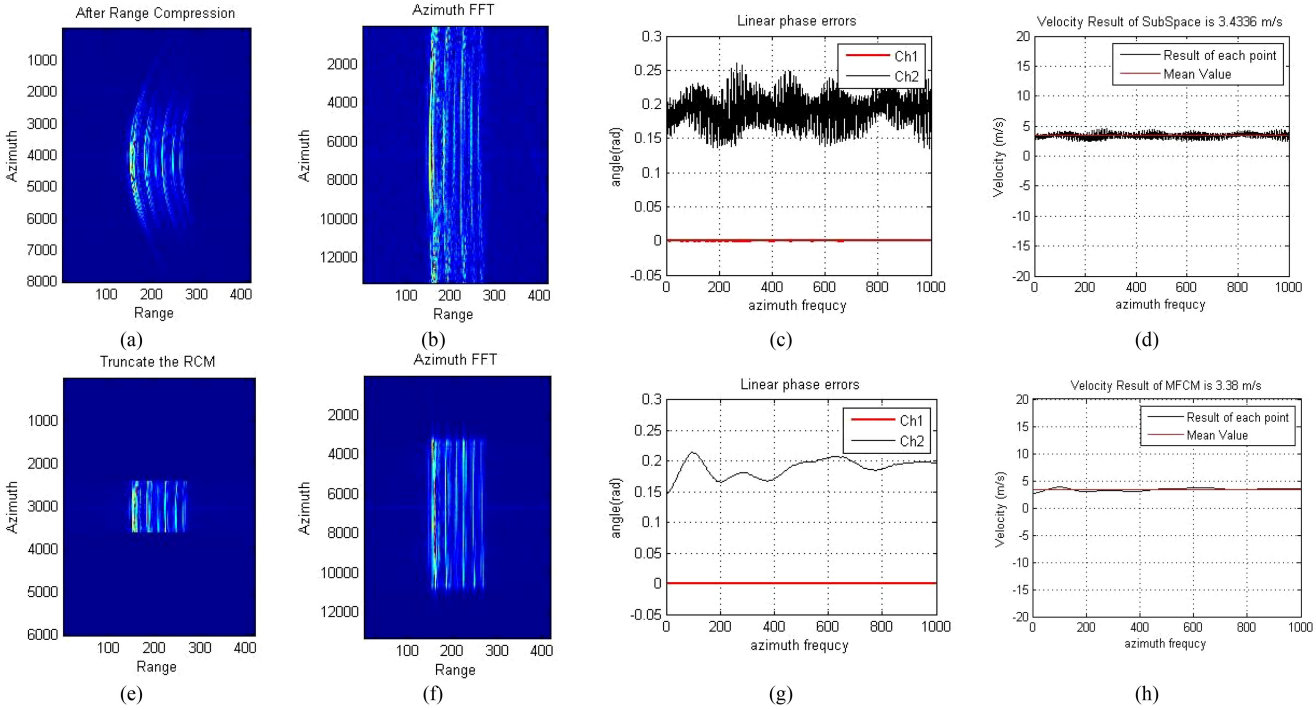

Fig. 7. SBM. (a) Truncation of the moving target after RC. (b) Azimuth spectrum of the moving target. (c) Linear phase errors estimated by SBM. (d) Mean radial velocity of 1000 Doppler bins, $v_r = 3.43$ m/s. MFCM. (e) Truncation of the RCM curve. (f) Azimuth spectrum of truncated moving target. (g) Linear phase errors estimated by MFCM method. (h) Mean radial velocity of 1000 Doppler bins, $v_r = 3.38$ m/s.

TABLE II
ESTIMATED RADIAL VELOCITY

	SBM	MFCM	SCR
Ship1	3.25m/s	3.28m/s	18.25dB
Ship2	2.97m/s	2.89m/s	17.03dB
Ship3	3.44m/s	3.40m/s	24.45dB
Ship4	2.56m/s	2.46m/s	24.07dB
Ship5	3.43m/s	3.38m/s	17.11dB
Ship6	4.05m/s	4.12m/s	21.65dB
Ship7	5.74m/s	5.98m/s	20.87dB

TABLE III
PARAMETERS OF THE SIMULATION SYSTEM

Symbol	Parameter	Value
λ	Wavelength	0.055517m
B_r	Signal bandwidth	120MHz
F_s	Sampling rate	150MHz
T_r	Pulse width	30μs
N	Channel number	6
d	Baseline	1.5m
v_s	Platform velocity	7500m/s
R_0	Reference slant range	800Km
f_r	PRF	1340.7Hz
B_a	Doppler bandwidth	5362.9Hz

C. Moving Target Imaging

Due to the unknown radial motion of the target, there will be noticeable position offset and ambiguity components in the SAR image, which makes the image difficult to interpret. For the sake of illustrating this phenomenon, the 7th moving target is enlarged, as shown in the yellow box in Fig. 6(a). The ambiguity components are in the red circles. In the azimuth multichannel SAR system, the critical role of radial velocity estimation is to suppress the ambiguity of moving targets. After the phase compensation [17], the mislocated is corrected and the false targets are suppressed, just as illustrated in Fig 6(b). Since the difference between the estimated results of the two methods does not exceed 0.1 m/s, only the estimated values from SBM are employed as the motion parameters to compensate for the phase. The effective suppression of azimuth ambiguity verifies the correctness of the velocity estimation results from another perspective.

V. PERFORMANCE ANALYSIS

A. Root-Mean-Squared Error

In this section, RMSE measures the accuracy of the radial velocity estimation by Monte Carlo simulations. To analyze performances more convincingly, we apply an additional simulated six-channel system operating in C-band, whose parameters are listed in Table III. Assuming that the number of Monte Carlo experiments is expressed as N_{mc}, then RMSE is calculated as

$$\sigma_{rmse} = \sqrt{\frac{1}{N_{mc}} \sum_{l=1}^{N_{mc}} \left(\widehat{v_r^l} - v_r \right)^2} \tag{39}$$

where $\widehat{v_r^l}$ represents the estimated value of the lth trial. And 500 Monte Carlo trials are conducted in the simulation under each condition. The RMSE of the SBM and MFCM is presented in

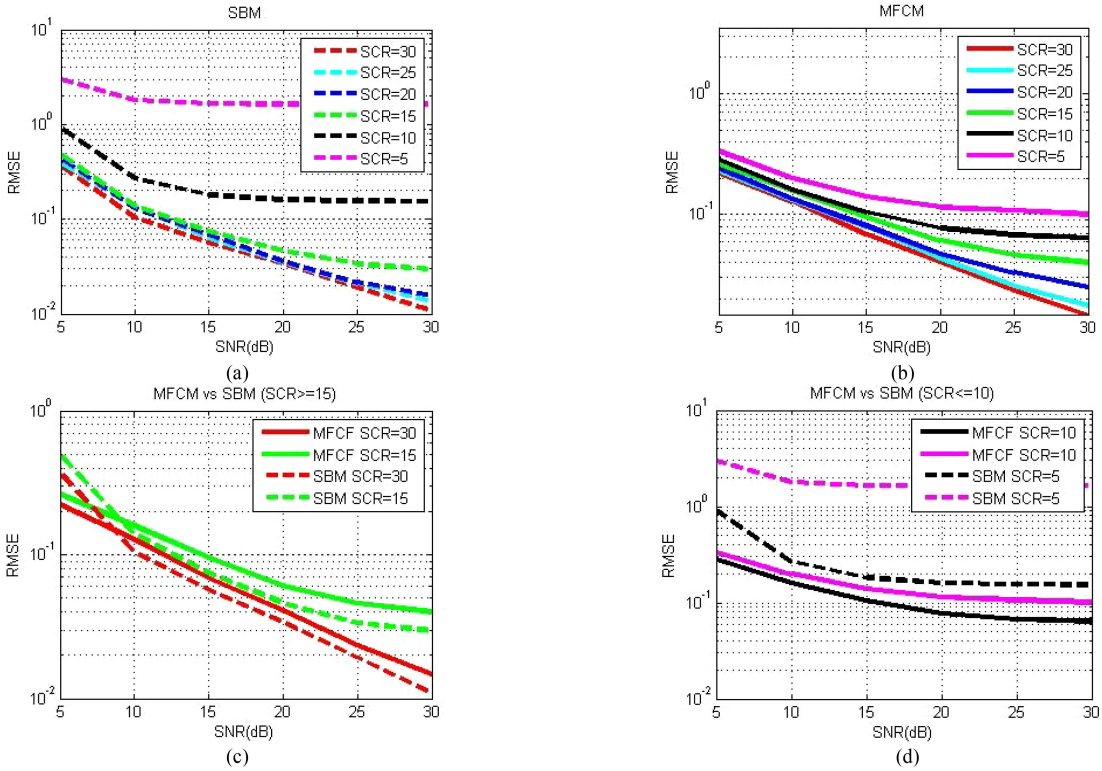

Fig. 8. (a) RMSE of the estimated radial velocity by the SBM. (b) RMSE of the estimated radial velocity by the MFCM. (c) Comparison of two methods when SCR $\geq$ 15 dB. (d) Comparison of two methods when SCR $\leq$ 10 dB.

Fig. 8(a) and (b). Moreover, the noise energy and clutter energy are measured in the RC domain. From the results, the estimation errors of the two methods are less than 0.1 m/s when the noise energy and clutter energy are relatively low, i.e., $\mathrm{SCR} > 15$ dB and $\mathrm{SNR} > 15$ dB. It is easy to meet this condition for large ships on the open sea in the RC domain. And the estimation accuracy of the SBM is higher than that of MFCM in such a situation from Fig. 8(c). In the real data experiment of Section IV, the clutter energy is relatively low from Table II. Therefore, we believe that the estimation results of the SBM are more reliable. Unfortunately, when the ship is small or the sea condition is poor, the energy of clutter will be relatively high. In this situation, the MFCM shows strong anti-interference performance, which is indicated in Fig. 8(d).

In summary, for the general large ships on the open sea, the estimation result of SBM is more accurate than that of MFCM. Once the clutter or noise energy cannot be ignored, MFCM shows better estimation performance. In addition, for SBM, at least one channel redundancy is required as the degree of freedom of the noise subspace, while MFCM does not have this limitation. Given the more comprehensive application range of the MFCM, we use it to explore the adverse effects of channel imbalance on radial velocity estimation without losing generality.

B. *Influence of Channel Imbalance*

In this article, the phase term introduced by motion is modeled as equivalent linear phase errors. The premise of estimating radial velocity is to compensate for the phase errors between channels in advance. In practice, it is almost impossible to eliminate the influence of phase errors between channels completely. The uncompensated part of channel imbalance is known as residual phase errors (RPEs) there. The q° RPE is modeled as a random distribution between $-q^\circ$ and q°. Fig. 9 tells the estimation error of radial velocity when the RPE ranges from 1° to 20°. When exploring the influence of a certain RPE level, 100 groups of phases are generated randomly. Then, the accuracy of the estimator is evaluated by the RMSE. From Fig. 9, every 10° RPE will introduce about 0.65 m/s estimation error. Consequently, the effect of RPE is much more significant than that of clutter and noise.

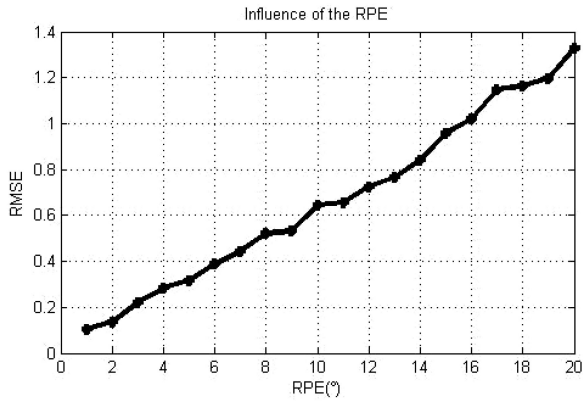

Fig. 9. Influence of the RPEs on radial velocity estimation.

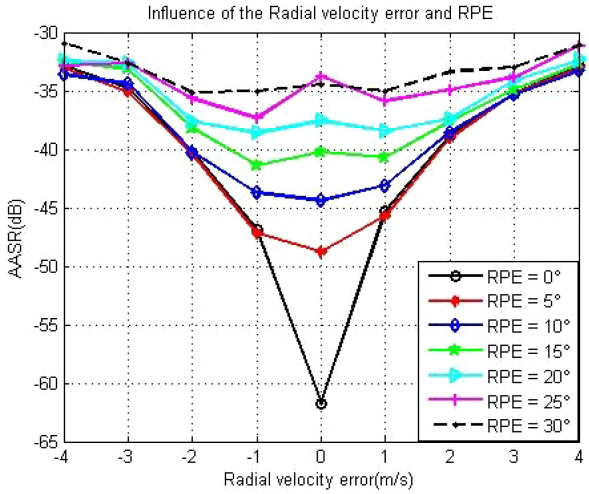

Fig. 10. Influence of the RPEs and velocity error on imaging quality.

One of the significant functions of velocity estimation is to suppress the azimuth ambiguity of moving targets. Thus, we apply the azimuth ambiguity-to-signal ratio (AASR) to evaluate the imaging quality, i.e.,

$$\mathrm{AASR} = 10 \cdot \log \frac{P_a}{P_s} \tag{40}$$

where P_a is the maximum power of the ambiguous target and P_s is the power of the real one. As a general rule, both the RPE and the phase term introduced by motion will affect the image quality, which is shown in Fig. 10. Every curve in different colors represents the image quality under various estimation errors when a certain level of RPE is added. The ideal situation is that the RPE is eliminated during preprocessing, and there is no error in the radial velocity estimation so that the AASR of the moving target is below -60 dB. In general, if the AASR is less than -45 dB, the false targets will be submerged in the clutter so as not to affect the image quality. Without the participation of RPE, image quality has a high tolerance for radial velocity estimation errors. If the echoes are superimposed with 5° RPE, the smaller the speed estimation error, the better the image quality. This conclusion can also be obtained from the curve with 10° RPE. In contrast, for the case that the RPE is larger than 10°, the image quality will deteriorate even if there is no velocity estimation error. Accordingly, if the RPE is larger, the main factor leading to the deterioration of the image quality is no longer the phase term caused by the target movement but the phase error between channels. In this case, the improvement of image quality mainly relies on compensating the channel imbalance to ensure the correct estimation of the radial velocity of the moving target.

VI. Conclusion

Azimuth multichannel SAR has been an important technology to produce an image of HRWS. And the estimation of moving target parameters is a critical research topic. The difficulty of radial velocity estimation in the azimuth multichannel SAR system lies in the under-sampling caused by the low PRF of each channel, which makes many traditional methods no longer applicable. This article proposes two algorithms of radial velocity estimation, namely the SBM and the MFCM. The basic idea is that the velocity estimation is converted into the linear phase errors estimation. The advantages in common are free from the iterative process and making full use of multichannel information. They also have their irreplaceable roles. For the SBM, as long as the energy of the moving ship is strong enough, the estimation result has higher accuracy. However, this method requires at least one channel to be redundant, that is, the Doppler ambiguity number must be less than the number of channels. As for the MFCM, its excellent anti-interference ability makes it have great application value. And the Doppler ambiguity number does not restrict its practical application. In addition, the velocity estimation is greatly affected by the RPEs between channels. If we only regard image quality as the criterion for judgment, we hope to control the RPEs within 10° as much as possible. Otherwise, priority should be given to the compensation for the channel imbalance.

References

[1] N. Gebert, G. Krieger, and A. Moreira, "Digital beamforming on receive: Techniques and optimization strategies for high-resolution wide-swath SAR imaging," *IEEE Trans. Aerosp. Electron. Syst.*, vol. 45, no. 2, pp. 564–592, Apr. 2009.

[2] A. Currie and M. A. Brown, "Wide-swath SAR," *IEE Proc. F, Radar Signal Process.*, vol. 139, no. 2, pp. 122–135, Apr. 1992.

[3] I. Sikaneta, C. H. Gierull, and D. Cerutti-Maori, "Optimum signal processing for multichannel SAR: With application to high-resolution wide-swath imaging," *IEEE Trans. Geosci. Remote Sens.*, vol. 52, no. 10, pp. 6095–6109, Oct. 2014.

[4] R. Werninghaus and S. Buckreuss, "The TerraSAR-X mission and system design," *IEEE Trans. Geosci. Remote Sens.*, vol. 48, no. 2, pp. 606–614, Feb. 2010.

[5] L. C. Morena, K. V. James, and J. Beck, "An introduction to the RADARSAT-2 mission," *Can. J. Remote Sens.*, vol. 30, no. 3, pp. 221–234, Jan. 2004.

[6] Y. Kankaku, S. Suzuki, and M. Shimada, "ALOS-2 first year operation result," in *Proc. IEEE Int. Geosci. Remote Sens. Symp.*, Jul. 2015, pp. 4121–4124.

[7] B. Han *et al.*, "The GF-3 SAR data processor," *Sensors*, vol. 18, no. 3, Mar. 2018, Art. no. 835.

[8] K. Tomiyasu, "Image processing of synthetic aperture radar range ambiguous signals," *IEEE Trans. Geosci. Remote Sens.*, vol. 32, no. 5, pp. 1114–1117, Sep. 1994.

[9] Z. Li, Z. Bao, H. Wang, and G. Liao, "Performance improvement for constellation SAR using signal processing techniques," *IEEE Trans. Aerosp. Electron. Syst.*, vol. 42, no. 2, pp. 436–452, 2006.

[10] T. Yang, Z. Li, Y. Liu, and Z. Bao, "Channel error estimation methods for multichannel SAR systems in azimuth," *IEEE Geosci. Remote Sens. Lett.*, vol. 10, no. 3, pp. 548–552, May 2013.

[11] M. Shang *et al.*, "The space-time variation of phase imbalance for GF-3 azimuth multichannel mode," *IEEE J. Sel. Top. Appl. Earth Observ. Remote Sens.*, vol. 13, pp. 4774–4788, Aug. 2020.

[12] T. Yang, Z. Li, Z. Suo, Y. Liu, and Z. Bao, "Performance analysis for multichannel HRWS SAR systems based on STAP approach," *IEEE Trans. Geosci. Remote Sens.*, vol. 10, no. 6, pp. 1409–1413, Nov. 2013.

[13] G. Krieger, N. Gebert, and A. Moreira, "Unambiguous SAR signal reconstruction from nonuniform displaced phase center sampling," *IEEE Trans. Geosci. Remote Sens.*, vol. 1, no. 4, pp. 260–264, Oct. 2004.

[14] J. K. Jao, "Theory of synthetic aperture radar imaging of a moving target," *IEEE Trans. Geosci. Remote Sens.*, vol. 39, no. 9, pp. 1984–1992, Sep. 2001.

[15] R. P. Perry and R. C. Dipietro, "SAR imaging of moving targets," *IEEE Trans. Aerosp. Electron. Syst.*, vol. 35, no. 1, pp. 188–200, Feb. 1999.

[16] S. A. S. Werness, W. G. Carrara, L. S. Joyce, and D. B. Franczak, "Moving target imaging algorithm for SAR data," *IEEE Trans. Aerosp. Electron. Syst.*, vol. 26, no. 1, pp. 57–67, Jan. 1990.

[17] J. Yang, X. Qiu, L. Zhong, M. Shang, and C. Ding, "A simultaneous imaging scheme of stationary clutter and moving targets for maritime scenarios with the first Chinese dual-channel spaceborne SAR sensor," *Remote Sens.*, vol. 11, no. 19, Sep. 2019, Art. no. 2275.
[18] S. Zhang, M. Xing, X. Xia, R. Guo, Y. Liu, and Z. Bao, "Robust clutter suppression and moving target imaging approach for multichannel in azimuth high-resolution and wide-swath synthetic aperture radar," *IEEE Trans. Geosci. Remote Sens.*, vol. 53, no. 2, pp. 687–709, Feb. 2015.
[19] T. M. Calloway and G. W. Donohoe, "Subaperture autofocus for synthetic aperture radar," *IEEE Trans. Aerosp. Electron. Syst.*, vol. 30, no. 2, pp. 617–621, Apr. 1994.
[20] D. E. Wahl, P. H. Eichel, D. C. Ghiglia, and C. V. Jakowatz, "Phase gradient autofocus—A robust tool for high resolution SAR phase correction," *IEEE Trans. Aerosp. Electron. Syst.*, vol. 30, no. 3, pp. 827–835, Jul. 1994.
[21] T. Jin, X. Qiu, D. Hu, and C. Ding, "Unambiguous imaging of static scenes and moving targets with the first Chinese dual-channel spaceborne SAR sensor," *Sensors*, vol. 17, no. 8, Jul. 2017, Art. no. 1709.
[22] S. Zhang, M. Xing, X. Xia, R. Guo, Y. Liu, and Z. Bao, "A novel moving target imaging algorithm for HRWS SAR based on local maximum-likelihood minimum entropy," *IEEE Trans. Geosci. Remote Sens.*, vol. 52, no. 9, pp. 5333–5348, Sep. 2014.
[23] S. V. Baumgartner and G. Krieger, "Simultaneous high-resolution wide-swath SAR imaging and ground moving target indication: Processing approaches and system concepts," *IEEE J. Sel. Top. Appl. Earth Observ. Remote Sens.*, vol. 8, no. 11, pp. 5015–5029, Nov. 2015.
[24] T. Jin, X. Qiu, D. Hu, and C. Ding, "An ML-Based radial velocity estimation algorithm for moving targets in spaceborne high-resolution and wide-swath SAR systems," *Remote Sens.*, vol. 9, no. 5, Apr. 2017, Art. no. 404.
[25] T. Yang, Y. Wang, and W. Li, "A moving target imaging algorithm for HRWS SAR/GMTI systems," *IEEE Trans. Aerosp. Electron. Syst.*, vol. 53, no. 3, pp. 1147–1157, Jun. 2017.
[26] Q. Wu, M. Xing, C. Qiu, B. Liu, Z. Bao, and T. Yeo, "Motion parameter estimation in the SAR system with low PRF sampling," *IEEE Geosci. Remote Sens. Lett.*, vol. 7, no. 3, pp. 450–454, Jul. 2010.
[27] Y. Shu, G. Liao, and Z. Yang, "Design considerations of PRF for optimizing GMTI performance in azimuth multichannel SAR systems with HRWS imaging capability," *IEEE Trans. Geosci. Remote Sens.*, vol. 52, no. 4, pp. 2048–2063, Apr. 2014.
[28] M. Dendrinos, S. Bakamidis, and G. Carayannis, "Speech enhancement from noise: A regenerative approach," *Speech Commun.*, vol. 10, no. 1, pp. 45–47, Apr. 1991.
[29] Y. Ephraim and H. L. Van Trees, "A signal subspace approach for speech enhancement," in *Proc. IEEE Int. Conf. Acoust., Speech, Signal Process.*, Apr. 1993, pp. 355–358.
[30] Fitting Linear Mixed-Effects Models. (n.d.).Mixed-Effects Models in S and S-PLUS, 133–199. doi: 10.1007/0-387-22747-4_4.
[31] J. Ward, "Space-time adaptive processing for airborne radar," MIT Lincoln Lab., Lexington, MA, USA, Tech. Rep., Dec. 1994, vol. 1015.

Junying Yang was born in Shanxi Province, China, in 1994. She received the B.S. degree in communication engineering from Harbin University of Technology, Weihai, China, in 2017. She is currently working toward the Ph.D. degree in signal processing and information science at the School of Electronic, Electrical and Communication Engineering, University of Chinese Academy of Sciences, Beijing, China.

She is trained by the Aerospace Information Research Institute, Chinese Academic of Sciences, Beijing, China. Her primary research interest focuses on azimuth multichannel synthetic aperture radar signal processing.

Xiaolan Qiu (Member, IEEE) received the B.S. degree in electronic engineering and information science from the University of Science and Technology of China, Hefei, China, in 2004, and the Doctoral Ph.D. degree in signal and information processing from the Graduate University of Chinese Academy of Sciences, Beijing, China, in 2009.

Since 2009, she has been with the Institute of Electronics, Chinese Academy of Sciences, Beijing, China. In 2011, she worked with the University of Siegen, Siegen, Germany, as a Visiting Scholar. She is currently a Research Fellow with Aerospace Information Research Institute (AIR) Beijing and AIR Suzhou. Her research interests include synthetic aperture radar (SAR) imaging and geo-correction, SAR simulation, SAR image interpretation, and SAR 3-D vision.

Mingyang Shang was born in Shandong Province, China, in 1993. He received the B.S. degree in electronic engineering from Shandong University, Jinan, China, in 2016. He is currently working toward the Ph.D. degree in signal processing and information science at the School of Electronic, Electrical and Communication Engineering, University of Chinese Academy of Sciences, Beijing, China.

He is trained by the Aerospace Information Research Institute, Chinese Academic of Sciences, Beijing, China. His primary research interest focuses on azimuth multichannel synthetic aperture radar signal processing.

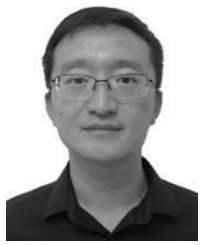

Shouye Lv was born in Shandong Province, China, in 1979. He received the Ph.D. degree in electronic engineering from the Beijing Institute of Technology, Beijing, China, in 2005.

He is with the Institute of Remote Sensing Information, Beijing, China. His primary research interest focuses on electronic signal processing.

Lihua Zhong received the B.S. degree in electronic engineering from Beihang University (BUAA), Beijing, China, in 2007, and the Doctoral Ph.D. degree in signal and information processing from the Graduate University of Chinese Academy of Sciences, Beijing, China, in 2013.

Since 2013, he has been with the Institute of Electronics, Chinese Academy of Sciences (IECAS), Beijing, China. He is currently an Associate Research Fellow with Aerospace Information Research Institute (AIR) Beijing. His research interests include synthetic aperture radar (SAR) imaging and radiometric correction, and SAR-GMTI/AMTI.

Chibiao Ding received the B.S. and Ph.D. degrees in electronic engineering from Beihang University, Beijing, China, in 1997.

Since 1997, he has been working with the Institute of Electronics, Chinese Academy of Sciences (IECAS), Beijing, China. He is currently a Research Fellow and Vice Director with Aerospace Information Research Institute (AIR), Beijing, China. His main research interests include advanced SAR systems, signal processing technology, information systems, and SAR 3-D vision.